Piezoelectric Microacoustic Metamaterial Filters

Onurcan Kaya, *Graduate Student Member, IEEE*, Xuanyi Zhao, *Graduate Student Member, IEEE*, and Cristian Cassella, *Member, IEEE*

***Abstract*—We present the first microacoustic metamaterial filters (MMFs). The bandpass of the reported MMFs is not generated by coupling, electrically or mechanically, various acoustic resonances; instead, it originates from the passbands and stopbands of a chain of three acoustic metamaterial (AM) structures. These structures form an AM transmission line (AMTL) and two AM reflectors (AMRs), respectively. Two single metal strips serve as input and output transducers with a wideband frequency response. Since MMFs do not rely on resonators, they do not require high-resolution trimming or mass-loading steps to accurately tune the resonance frequency difference between various microacoustic resonant devices. These steps often involve finely controlling the thickness of a device layer, with resolutions that can be as low as a few Angstroms when building GHz filters. The acoustic bandwidth of MMFs is mostly determined by geometrical and mechanical parameters of their AM structures. MMFs necessitate external circuit components for impedance matching, in contrast to the existing microacoustic filters that often employ circuit components only to eliminate ripples within their passband. We have designed and constructed the first MMFs from a 400-nm-thick scandium-doped aluminum nitride (AlScN) film using a 30% scandium-doping concentration. These devices operate in the radio frequency (RF) range. We validated these devices' performance through finite-element modeling (FEM) simulations and through measurements of a set of fabricated devices. When matched with ideal circuit components, the built MMFs exhibit filter responses with a center frequency in the ultrahigh-frequency range, a fractional bandwidth (FBW) of ∼2.54%, a loss of ∼4.9 dB, an in-band group delay between 70 ± 25 ns, and a temperature coefficient of frequency (TCF) of ∼22.2 ppm/°C.**

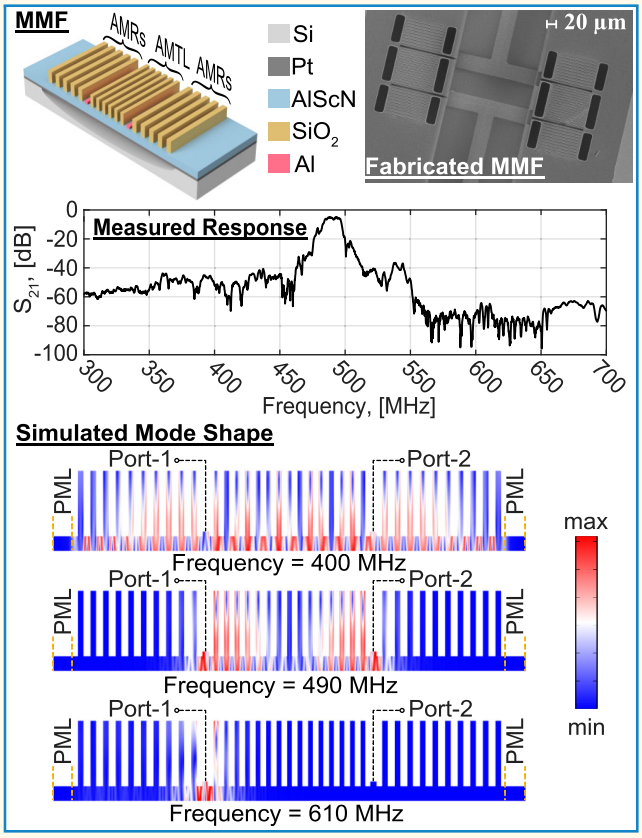

***Index Terms*— Aluminum scandium nitride, bulk acoustic wave (BAW) devices, piezoelectric metamaterials, radio frequency (RF) filters.**

Nomenclature

AlN	Aluminum nitride.
AlScN	Scandium-doped AlN.
AM	Acoustic metamaterial.
AMR	AM reflector.
AMTL	AM transmission lines.
AWLR	Acoustic-wave-lumped-element resonator.
Au	Gold.
BAW	Bulk acoustic wave.
CMOS	Complementary metal–oxide–semiconductor.
CVD	Chemical vapor deposition.
C_t	Capacitance of the input/output transducer.
C_{MN}	Capacitor used in MMF's matching network.
C_{MN}^{opt}	Required capacitance to ensure proper matching of MMF's terminal impedance to 50 Ω.
FBW	Fractional bandwidth.
f_c	Center frequency.
FEM	Finite-element modeling.
HR	High resistivity.
ICP-RIE	Inductively coupled plasma reactive ion etching.
k_t^2	Piezoelectric coupling coefficient.
L_{MN}	Inductor used in MMF's matching network.
L_{MN}^{opt}	Required inductance to ensure proper matching of MMF's terminal impedance to 50 Ω.
MMF	Microacoustic metamaterial filter.

Manuscript received 24 April 2024; accepted 21 July 2024. Date of publication 24 July 2024; date of current version 5 September 2024. This work was supported by the National Science Foundation (NSF) through CAREER Award under Grant 2034948. *(Corresponding author: Onurcan Kaya.)*

The authors are with the Department of Electrical and Computer Engineering, Northeastern University, Boston, MA 02115 USA (e-mail: kaya.on@northeastern.edu; zhao.xuan@northeastern.edu; c.cassella@northeastern.edu).

Digital Object Identifier 10.1109/TUFFC.2024.3432849

Highlights

- **AMTL and reflectors form an MMF with a steep skirt and a high out-of-band rejection.**
- **MMFs do not require resonating transducers. So, they do not need the high-resolution mass loading and trimming steps employed when building ladder filters.**
- **MMFs' center frequency is lithographically defined. Multiple MMFs can be built on the same chip without adding fabrication steps.**

$MMF^{(PML)}$	MMF whose AMRs are replaced with PMLs.
$MMF^{(SF)}$	MMF whose AMRs are replaced with stress-free boundaries.
p_{AMR}	Unit cell pitch of an AMR.
p_{AMTL}	Unit cell pitch of an AMTL.
PML	Perfectly matched layer.
Pt	Platinum.
Q	Quality factor.
RIE	Reactive ion etching.
R_{in}	Real part of MMF's input impedance.
$R_{OoB}{}^{(Left)} R_{OoB}{}^{(Right)}$	Average out-of-band rejection on the left-/right-hand side of the MMF's passband.
SAW	Surface acoustic wave.
$Sc_{\%}$	Scandium-doping concentration.
SEM	Scanning electron microscopy.
SiO_2	Silicon oxide.
TCF	Temperature coefficient of frequency.
VNA	Vector network analyzer.
2DRR	2-D resonant rod.

I. Introduction

OVER the last two decades, piezoelectric microacoustic filters have been essential components of commercial radio frequency (RF) front ends. These devices typically leverage the piezoelectric excitation of a set of acoustic resonances, electrically or mechanically coupled to generate bandpass filtering characteristics in their electrical frequency response. Due to the acoustic wavelength being orders of magnitude shorter than the electromagnetic one, microacoustic filters offer exceptional degrees of miniaturization [1], [2]. This is crucial for the current chip-scale multiband radios to maintain a compact form factor. AlN has been the most used piezoelectric material in cellular handsets over the last 30 years. This has been driven by the fact that AlN is low loss, has a wide bandgap, and can be processed using steps, materials, and temperature conditions available when building CMOS circuits. Only, recently, researchers worldwide have diverted their attention from AlN to scandium-doped AlN (or AlScN). AlScN shows higher piezoelectric coefficients than AlN when doped with high scandium-doping concentrations. This enables wider FBWs in microacoustic filters [3], [4], [5], [6], [7], [8], [9].

Regardless of the adopted piezoelectric material, there currently exist two main acoustic filter technologies: SAW filters [10], [11] and BAW filters [12], [13], [14], [15]. SAW and BAW filters differ in the acoustic modes they leverage to create their electrical passband. The former relies on the propagation of SAWs, while the latter relies on the propagation of BAWs. SAW and BAW filters are characterized by insertion loss, bandwidth, and frequency selectivity determined by the achievable electromechanical performance of their resonant structures (e.g., by material properties). They are often designed using a "ladder" arrangement, incorporating multiple one-port resonators that are electrically interconnected. These resonators must be designed, so that their resonance frequencies adhere to a precise relationship, which is key to ensure proper impedance matching. In practice, this can be a challenging task due to process variations and nonhomogeneity in the thickness of these resonators' forming layers. Postprocessing fabrication steps, such as mass loading and trimming, have allowed to overcome these challenges when manufacturing BAW ladder filters operating up to a few GHz, at the expense of higher manufacturing costs. Nevertheless, performing these procedures necessitates precise control over the thickness of a tuning layer within the body of these resonators. This task is challenging and becomes even more daunting when dealing with BAW filters operating in the mm-wave range. Such filters generally employ thinner resonators, demanding thickness resolutions that can be as low as a fraction of Angstroms during mass loading or trimming processes [16], [17]. The use of distinct resonators can also introduce large ripples in the group delay within ladder filters' passband [18]. These ripples affect radios' capability to accurately decipher information encoded in the phase of a received RF signal. The amplitude of these ripples increases proportionally with the filter order (i.e., coinciding with the number of resonators used) and quality factor (Q) of the resonators employed, while decreasing inversely with the resonators' electromechanical coupling coefficient (k_t^2). Alternative BAW filters using two-port Lamb wave resonators [19], [20], [21], [22] or acoustically coupled resonances [23], [24], [25], [26] have also been reported. Two-port Lamb wave resonators usually have narrower bandwidths compared with ladder filters. Also, their out-of-band rejection is worse than that of ladder filters. Acoustically coupled filters, on the other hand, provide wider bandwidths compared with ladder filters. However, their near-band selectivity is worse than that of ladder filters. These explain why both two-port Lamb wave resonators and acoustically coupled filters have not been considered for use in multiband RF front ends.

Hybrid filters formed by a set of identical microacoustic resonators coupled through electrical lumped components have also been proposed [18], [27], [28], [29], [30]. These filters, often referred to as "AWLR filters," can exhibit bandpass characteristics with relatively flat group delays [18], can be designed to have improved out-of-band isolation [27], or can

provide a reconfigurable transfer function [29]. AWLR filters employ replicas of identical microacoustic resonators, interconnected through cascaded networks of inductors and capacitors. Relying on copies of the same resonator relaxes the fabrication complexity with respect to conventional ladder filters using at least two different resonator types, at the expense of a significantly larger form factor and higher loss. AWLR filters can achieve broader passbands compared to those possible with only microacoustic devices, although their bandwidth is still limited by the k_t^2 of the resonators used. Unfortunately, these filters' response remain sensitive to process variations, affecting their microacoustic resonators. Also, their out-of-band rejection per filter stage is determined by the Q of the adopted lumped components, which typically does not exceed 120 for ceramic components. Consequently, AWLR filters typically necessitate multiple stages, resulting in higher insertion loss and a larger form factor. The described limitations of the existing microacoustic filter technologies motivate why the availability of a high-performance microacoustic filter not relying on resonators would be beneficial. However, achieving good out-of-band rejection without using high-Q resonators is one of the biggest challenges that needs to be tackled in developing such a desired filter component.

Recently, there has been a growing interest about AMs. AMs can generate effective material properties that are not readily available in nature, i.e., negative bulk modulus and/or negative mass density [31], [32], [33]. This unique feature enables new ways of controlling acoustic waves and paves the way for exotic applications, such as acoustic cloaking [34], [35], vibration isolation for MEMS structures [36], and imaging [37], [38]. Our group has also explored the potential of AMs embodying a piezoelectric layer to enhance the performance of BAW resonators operating in the RF range. Through our investigation, we have demonstrated a new class of RF resonators, namely, the 2DRR devices [39], [40]. The 2DRRs exploit a set of reactively coupled quasi-thickness modes of vibration. These modes are internally transduced within an AM structure composed of AlN or AlScN rods, deposited atop a Pt/AlN or Pt/AlScN bilayer. In another study, we have also shown how the same AM structure used by 2DRRs can be used as a *frequency-selective* anchor. This allows to confine the acoustic energy within the body of a contour-mode resonator even when a large anchoring volume is used along the main direction of motion. The use of a large anchoring volume eases the flow of heat generated during the motion into the surrounding substrate, allowing improved power handling capabilities [41].

In this article, we discuss the operation, the fabrication, and the performance of the first MMFs. MMFs construct a bandpass behavior by leveraging the dispersion of AMs made of a thin AlScN film and an array of SiO_2 rods. The reported MMFs are single stage, and they are formed by an AMTL placed between two AMRs. The reported MMFs also embody two single-electrode input and output transducers. When matched with two ideal circuit components (one inductor and one capacitor), the reported MMFs show a passband centered around 490 and 395 MHz, an FBW higher than 2.5%, a maximum insertion loss of 4.9 dB, and significant out-of-band rejection reaching ~75 dB.

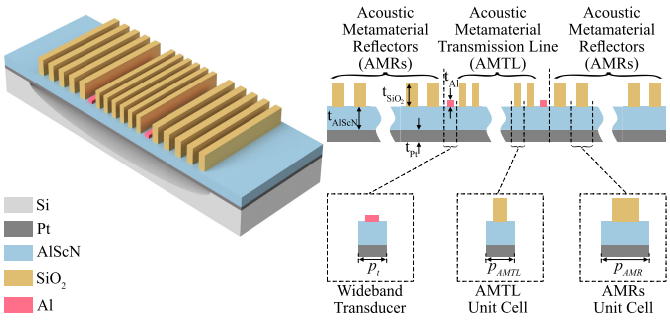

Fig. 1. Three-dimensional and cross-sectional view of an MMF, consisting of an AMTL, placed between two AMRs, and two transducers, one for the input and one for the output. Both the AMTL and the AMRs are formed by a combination of unit cells with different pitches (p_{AMTL} or p_{AMR}). Each unit cell consists of a SiO_2 rod atop an $Al_{0.7}Sc_{0.3}N$/Pt bilayer.

In Section II, we will first discuss the operating principles of MMFs. Then, in Section III, we will describe their fabrication process and provide the results of our experimental validation. We will also show how MMFs allow a lithographic control of their center frequency.

II. Principle of Operation

AMs are formed by chains of identical unit cells. When built in suspended plates, they can inhibit the propagation of Lamb modes within certain frequency ranges often referred to as stopbands. The center frequency and width of these stopbands are determined by mechanical and geometric properties of the AMs' unit cell. Between adjacent stopbands, there exist one or more propagating modes that can be leveraged to guide acoustic energy across AMs' structure.

MMFs are formed by an AMTL constructed between two transducers, one for the input and one for the output, and two AMRs. The AMRs are affixed to the surrounding substrate. The combination of AMTL and AMRs creates zones of significant attenuation near the targeted filter passband. Within these zones, the propagation of longitudinal and shear waves is either blocked or heavily damped, resulting into a large out-of-band rejection, although no resonator is used. The AMTL and the AMRs are formed by the same material stack, which includes a set of silicon dioxide (SiO_2) rods deposited atop a thin AlScN film. The rods' longest dimension is orthogonal to MMFs' cross section. A schematic of an MMF is reported in Fig. 1. Both the AMTL and the AMRs consist of a chain of unit cells with pitch being twice the width of the rods. In the following, we will refer to the pitch values of the AMTL's and AMRs' unit cells as p_{AMTL} and p_{AMR}, respectively. The input and output transducers are formed by single aluminum (Al) strips. Applying a voltage between the input transducer and ground permits to transduce a longitudinal BAW along the AMTL's width. This transduction leverages the d_{31} piezoelectric coefficient of AlScN. The same coefficient is leveraged by the output transducer to convert the strain under the output terminal into a voltage. The AMTL and AMRs serve distinct purposes in the operation of MMFs.

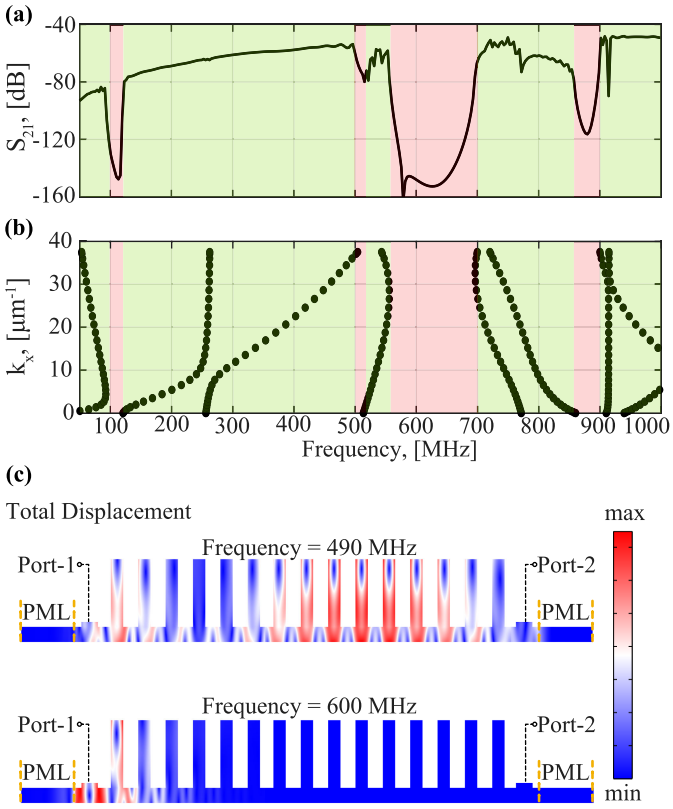

Fig. 2. FEM analysis of the AMTL. (a) S_{21} response of the AMTL, showing five passbands (highlighted in green) and four stopbands (highlighted in red). (b) Dispersion curves of the AMTL's unit cell assuming Floquet boundary conditions at its two ends. (c) Total displacement modeshapes of the AMTL operating within a passband (at 490 MHz) or a stopband (at 600 MHz).

We describe their role in Sections II-A–II-C, elucidating on how their interaction allows to generate MMFs' passband and enables their frequency selectivity.

A. AM Transmission Lines

AMTLs are pivotal in MMFs' functionality. Their unique acoustic dispersion allows to create complete stopbands right above the desired passband, blocking the propagation of longitudinal and shear waves along the MMFs' lateral direction. In these stopbands, acoustic real power cannot flow along the MMFs' width, restricting the electrical power transmission between input and output transducers to a minimal value that is solely determined by electrostatic feedthrough. In order to visualize the operation of an AMTL and the origin of their stopbands, we run a set of FEM simulations. We have assumed an AMTL embodying 15 unit cells, with a p_{AMTL} of 5 μm and a length of 80 μm. Each unit cell of the AMTL includes a SiO_2 rod with a thickness of 2.2 μm and a width of 2.5 μm. The rods are located atop a 400-nm AlScN layer that uses a 30% scandium-doping concentration ($Sc_{\%}$). We have also considered two 150-nm-thick aluminum (Al) strips as input (i.e., Port-1) and output (i.e., Port-2) transducers, such as our experiments. All the geometrical parameters considered in our simulations coincide with dimensions used by the first built MMF prototype presented in this work. We have also assumed two PMLs along the lateral sides of the simulated AMTL to prevent distortions in acoustic transmission due to scattering and mode conversion at stress-free surfaces. In practice, these effects do not impact the built MMFs' performance, as these devices are fully anchored along their lateral sides.

We started our FEM simulations by monitoring the S_{21} scattering parameter [see Fig. 2(a)], which maps the transmission of electrical power from Port-1 (i.e., from the input transducer) to Port-2 (i.e., to the output transducer) when these ports are terminated with 50-Ω loads. We found the existence of four bands with greatly reduced S_{21} magnitudes. These bands are stopbands of the AMTL structure, wherein the transmission of acoustic (thus electric) power from the input port to the output port is blocked. This has been verified by running a second set of FEM simulations [see Fig. 2(b)]. In this second round of simulations, we looked at the dispersion curves of the AMTL's propagating modes with frequency included within the same frequency range analyzed in Fig. 2(a). Each one of these curves has been drawn [see Fig. 2(b)] in terms of the corresponding mode's lateral wavevector (k_x) versus frequency. To run this second round of FEM simulations, we have used Floquet boundary conditions at both the sides of the unit cell. We have also examined the modeshape of the total displacement distribution across the cross section of the AMTL when this device is electrically driven at various frequencies from its input terminal. In this context, Fig. 2(c) shows the simulated modeshape when the input frequency is within a passband (490 MHz) or a stopband (600 MHz). In the first scenario, a significant amount of acoustic energy is transmitted from the input port to the AMTL's output port, whereas the total displacement in the second scenario is heavily dampened after passing through the first four unit cells from the input terminal.

Looking at Fig. 2(a), it is easy to realize that the S_{21} is flat from 475 to 500 MHz, while showing a large suppression for frequencies higher than 500 MHz. It is reasonable to question whether these two aspects can be leveraged to reconstruct the frequency response of a bandpass filter with center frequency included between 475 and 500 MHz. In this regard, one can leverage the stopbands centered at 530 and 650 MHz to provide an out-of-band rejection higher than 100 dB after matching the input and output terminals to the optimal termination. The high attenuation in AMTLs' stopbands is attained even though no high-Q resonator is used. This is a novel finding that prior microacoustic filters could not exploit. Nonetheless, using the unique dispersion of the AMTL to form a filter with a passband ranging from 475 to 500 MHz requires creating another area of significant attenuation for frequencies below 475 MHz. This can be done by using two AMRs, as discussed in Section II-B.

B. AM Reflectors

The AMRs used by MMFs are utilized as frequency selective reflectors. They facilitate the lateral transmission of acoustic power from the transducers to the neighboring silicon substrate within their passbands, while impeding it within their stopbands. During the design of MMFs, the AMRs must be designed in conjunction with the AMTL, so that their deepest stopband covers the desired filters' passband. This requires

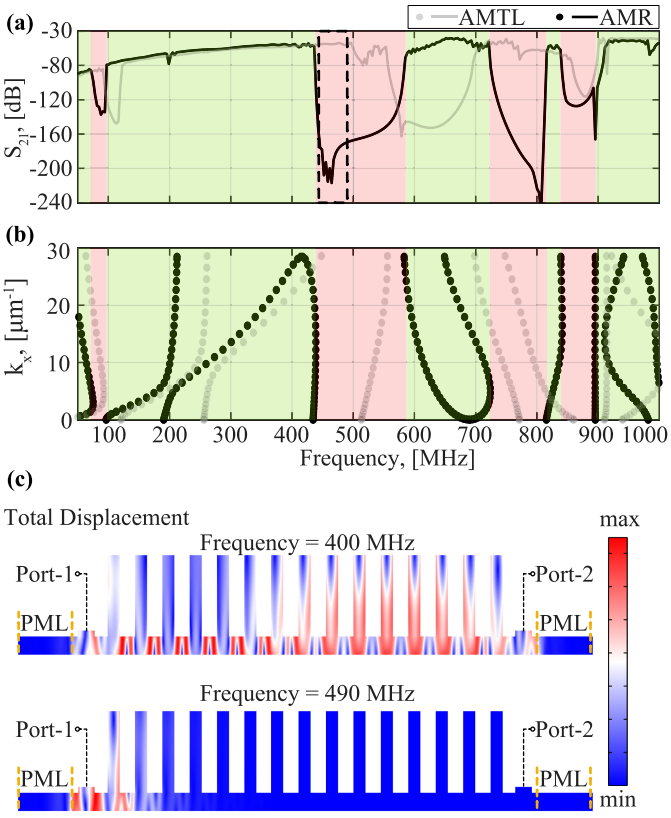

Fig. 3. FEM analysis of an AMR. (a) S_{21} response of one AMR, showing five passbands (highlighted in green) and four stopbands (highlighted in red). (b) Dispersion curves of the unit cell of the AMR when assuming Floquet boundary conditions at its two ends. (c) Total displacement modeshapes of the AMR when operating within a passband (at 400 MHz) or a stopband (at 490 MHz).

using a p_{AMR} value different from p_{AMTL}. In fact, the center frequency of each stopband for all the AM structures described in this article can be lithographically changed by varying the pitch of their unit cells. We can use the AMRs' wide passband region below their most significant stopband to enable a large radiation of acoustic energy into the surrounding substrate for frequencies lower than the targeted filter's passband. This comes with a large attenuation of the acoustic power reaching the output terminal, which results in a strong reduction of the S_{21} for frequencies below the targeted filter's passband. This allows to reconstruct the typical S_{21} versus frequency trend of a bandpass filter after matching the input and output terminals to the optimal termination.

As a numerical example, we used FEM simulations to design a set of AMRs that can be connected to the AMTL structure discussed in Fig. 2 to achieve a bandpass filtering behavior from 475 to 500 MHz. As done for the AMTL structure, we run two sets of FEM simulations. The first set aimed at assessing the transmission properties of an AMR at different input frequencies. For these simulations, we considered the same materials, transducers, and PML boundaries used for Fig. 2. However, we employed a different pitch (i.e., $p_{\text{AMR}} = 6$ μm) for the analyzed AM structure placed between the two terminals. This is the same pitch value we have used for the AMRs in our experiments. We report in Fig. 3(a) the extracted S_{21} versus frequency trend for the FEM-simulated AMR structure. Fig. 3(a) also reintroduces the S_{21} versus frequency trend of the AMTL structure for an easier visualization of the key design differences between the AMRs and the AMTL. As for the AMTL discussed in Fig. 2, we have also run a second set of FEM simulations [see Fig. 3(b)]. These simulations have confirmed that the large attenuation in the S_{21} versus frequency trend of the AMRs originates from the presence of stopbands in the AMRs' acoustic frequency response. Finally, the modeshape of the total displacement within the analyzed AMR structure is also reported for two frequencies, one in a passband and one in the widest stopband. Similar to the AMTL described in Section II-A, the analyzed AMR shows a significant total displacement for the first case and a negligible one for the second case.

C. MMF—Performance Bounds

In Sections II-A and II-B, we have discussed the principle operation and design criteria for the AMTL and the AMRs. In this section, we discuss the overall performance achievable by MMFs using such AM-based components. As previously noted, the combined use of an AMTL and two AMRs enables the creation of two broad frequency regions, wherein the acoustic power flowing from the input transducer of the MMF to the output transducer is significantly attenuated. The presence of these two regions reshapes the spectrum of the AMTL's acoustic transmission. As a result, MMFs' electrical transmission reconstructs the typical behavior of a bandpass filter when MMFs' terminals are properly matched to optimal terminations. The value of these terminations ultimately depends on the capacitance of the input and output transducers, C_t. The larger the C_t, the closer the real part of MMFs' input impedance (R_{in}) approaches 50 Ω. R_{in} is directly associated with the radiation resistance of MMFs' input and output transducers. Since MMFs do not rely on resonators for electrical matching, they require two matching networks to cancel the capacitive behavior of their input and output transducers. These matching networks can be synthesized by using networks of inductors and capacitors, arranged using a circuit topology that strictly depends on C_t.

We recur to a case study to analyze the impact of C_t and the required matching network on MMFs' performance. Specifically, we look at the same design case we have considered in Sections II-A and II-B (i.e., the design of filter, with passband extending from 475 to 500 MHz, using the AMTL and AMRs described in Figs. 2 and 3). For this case, a matching network per terminal can be used to match the input and output transducers for a broad range of C_t values [see Fig. 4(a)]. Each one of these networks relies on one inductor (L_{MN}) and one capacitor (C_{MN}). We have analyzed the impact of these matching networks on MMFs' filter performance through combined FEM + circuit simulations. The plot in Fig. 4(b) shows the trend of the required L_{MN} ($L_{\text{MN}}^{\text{opt}}$) and C_{MN} values ($C_{\text{MN}}^{\text{opt}}$) versus C_t to ensure proper matching of the input and the output terminals to 50 Ω. In Fig. 4(c), we plot the simulated loss that MMFs experience due to ohmic dissipations in the matching networks. This loss has been computed for the same C_t values analyzed in Fig. 4(b) when assuming L_{MN} and C_{MN} to be equal to $L_{\text{MN}}^{\text{opt}}$ and $C_{\text{MN}}^{\text{opt}}$, respectively. All the

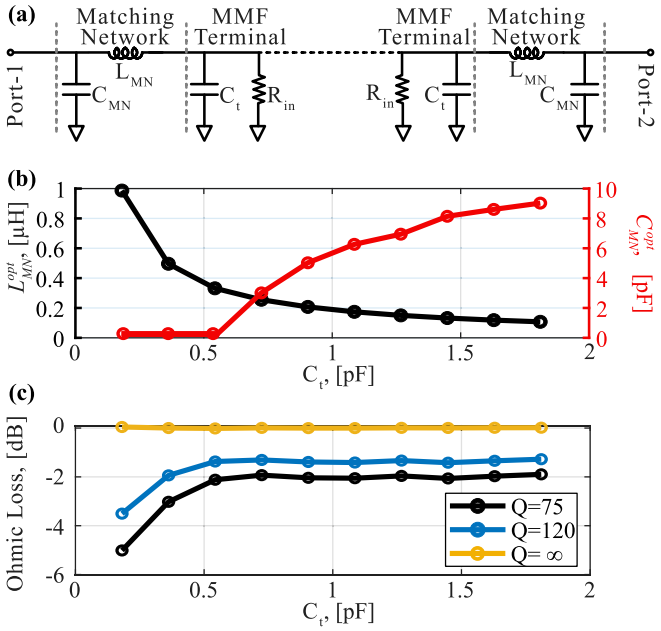

Fig. 4. Impact of the required matching networks on MMFs' performance. (a) Circuit schematic showing the lowest order matching networks that can be used to match MMFs' input and output transducers to 50 Ω. (b) Required inductance (in black) and capacitance (in red) versus C_t to ensure proper matching of MMFs' transducers to 50 Ω. (c) Ohmic loss caused by the two required matching networks (one per port) for varying C_t values, when assuming a Q of 75, 150, or infinity for the matching inductors.

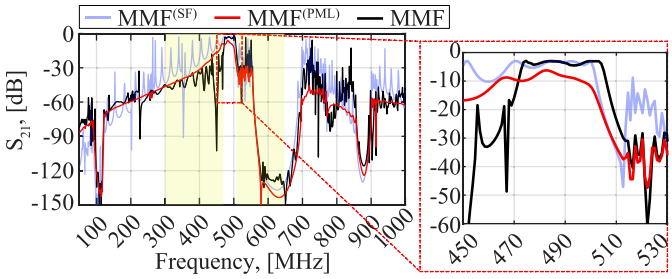

Fig. 5. FEM-simulated insertion loss of MMF (black curve), MMF^{PML} (red curve), and MMF^{SF} (blue curve) when their input and output transducers are matched to 50 Ω through optimal matching components [L_{MN} = 496 nH, and C_{LM} = 0.1 pF; see Fig. 4(a)] having a Q equal to 75 (the highlighted regions have been used to extract the average out-of-band rejection values reported in Fig. 7).

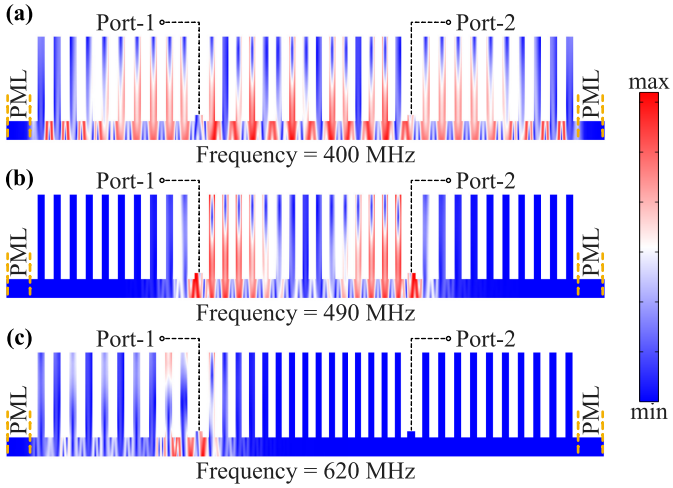

Fig. 6. Total displacement modeshapes of an MMF using the AMTL discussed in Fig. 2 and two copies of the AMR discussed in Fig. 3 for (a) frequency (400 MHz) included in the AMRs' passband, (b) frequency (490 MHz) included in the AMRs' stopband, and (c) frequency (620 MHz) inside the deepest stopband of the AMTL.

trends shown in Fig. 4(b) and (c) were found by assuming a Q for all the inductors equal to 75 (the same Q of the inductors used in the AWLR filters reported in [27]), 120 (i.e., the highest Q value for ceramic inductors), or infinity (i.e., corresponding to the case of lossless matching networks). In summary, the simulation data shown in Fig. 4 suggest that larger C_t values allow a lower impact of the matching networks on the performance of MMFs. In other words, for large C_t values, MMFs' filtering performance is mostly determined by acoustic losses in their AM structures.

Since it is desirable to have large C_t values, it is important to identify methods to meet this design requirement. Two approaches can be followed. One approach consists of widening the input and output transducers' size. However, increasing the size of these transducers too much may cause undesired generation of stationary waves confined within the transducers' region, causing distortions in MMFs' filter passband. In turn, making the transducers too long would increase the electrical loading. Another approach to increase C_t without risking of introducing spurious modes in MMFs' passband consists of stacking multiple MMF devices with input and output terminals in parallel with each other. For our experimental validation, we have followed the latter approach, as discussed in Section III.

Fig. 5 presents the FEM-simulated S_{21} response (see the black curve) of an MMF with two devices stacked in parallel, mirroring our experimental setup. This figure utilizes the same AMTL and AMRs described in Figs. 2 and 3. Also, similar to Sections II-A and II-B, a 30% $Sc_{\%}$ was considered for this FEM simulation, together with a value for the total input and output capacitances (equal to $2C_t$) of 0.36 pF, and a Q of 75 for the matching inductors. Fig. 5 also includes two other S_{21} trends. One trend refers to the transmission of the same MMF if one replaces the AMRs with stress-free boundaries (MMF^{SF}) (see the blue curve). The other trend shows the S_{21} when replacing the AMRs with PML (MMF^{PML}). Evidently, the adoption of the AMRs allows the formation of the MMF's passband. Also, it prevents the excitation of plate modes that are, otherwise, transduced when stress-free boundaries are used. At the same time, AMRs improve both the frequency selectivity and the insertion loss compared with the case where PMLs are used. It is also worth emphasizing that the biggest stopband on the right-hand side of MMF's passband allows to achieve an out-of-band rejection higher than 120 dB. Such a high rejection value, attained relatively close to the MMF's passband, is hardly achievable by AWLR filters, since their skirt steepness is limited by the smooth dispersion of lumped capacitors. Fig. 6 shows the total displacement modeshapes of the MMF discussed in Fig. 5 when this is driven at various frequencies. One driving frequency is included in the passband of the MMF's adopted AMRs [see Fig. 6(a)], producing a large displacement across the entire device. Another frequency

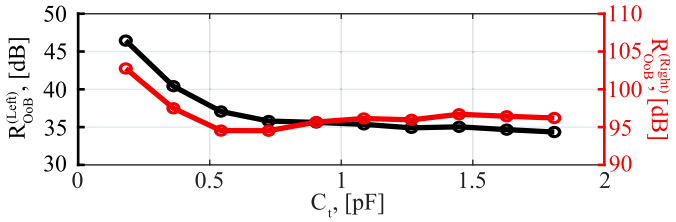

Fig. 7. Average out-of-band rejection on the left-hand (in black) and right-hand (in red) sides of the MMF's passband. The frequency ranges considered for this computation are shown in Fig. 5.

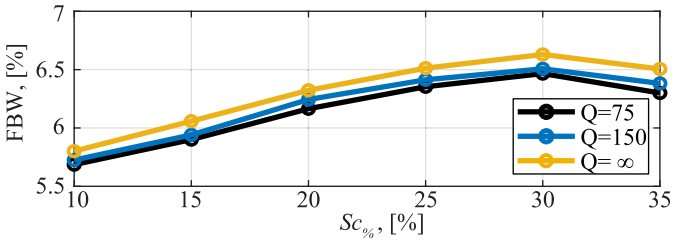

Fig. 8. Impact of $Sc_{\%}$ on MMFs' FBW. FEM-simulated FBW for the MMF reported in Fig. 4 when considering different $Sc_{\%}$ values and different Q values for the matching inductors.

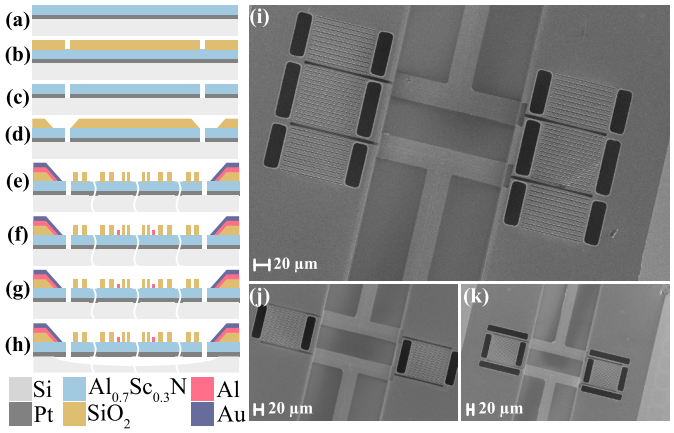

Fig. 9. (a)–(h) Fabrication flow of the MMF and (j)–(l) SEM images of the fabricated devices. (a) Fabrication started by sputtering Pt and AlScN on top of an HR Si wafer. (b) SiO_2 was deposited and patterned for use as a hard mask during the formation of the release windows. (c) Release windows were etched using ICP-RIE. (d) Another layer of SiO_2 was patterned under the pads to decrease the parasitic capacitance due to routing. (e) Same oxide layer was then patterned again to form the rods. (f) Al electrodes were deposited. (g) Au probing pads were deposited. (h) Device was released using XeF_2 isotropic etch. SEM pictures of the fabricated devices: (j) MMF, (k) $MMF^{(PML)}$, and (l) $MMF^{(SF)}$.

[see Fig. 6(b)] is included within the MMF's passband, showing limited displacement across AMRs' width. The last frequency is included within the deepest AMTL's stopband on the right-hand side of MMF's passband [see Fig. 6(c)]. Evidently, at this last analyzed frequency, the acoustic wave is fully confined in the vicinity of the input transducer.

Finally, in Fig. 7, we report the average out-of-band rejection on both the left-hand ($R_{OoB}^{(Left)}$) and right-hand ($R_{OoB}^{(Right)}$) sides of the MMF's passband for varying C_t values. For this final study, we assumed the same matching networks considered in Fig. 4.

D. Impact of the Scandium-Doping Concentration

Another aspect worth analyzing is the dependence of MMFs' 3-dB FBW on the adopted $Sc_{\%}$. We report in Fig. 8, the trend of FBW versus $Sc_{\%}$ for the same case study considered in Fig. 4. Evidently, using higher $Sc_{\%}$ values does not significantly impact the achievable FBW. As a matter of fact, using a lower $Sc_{\%}$ reduces the elastic modulus of the piezoelectric layer, which affects the dispersion characteristics of both the AMTL and the AMRs. Since p_{AMTL} and p_{AMR} are different, the change in their acoustic dispersion produces a suboptimal overlap of the desired filter's passband with AMRs' stopband. This explains the minor variations of the simulated FBW value with different $Sc_{\%}$ values. It is also worth emphasizing that FBW does not depend significantly on the Q of the matching inductors, as also evident from Fig. 8.

III. Experiments and Analysis

A. Fabrication

To experimentally characterize the performance of MMFs, we microfabricated a set of devices. Each device captures the operation of an AMTL (see Fig. 2) and an AMR (see Fig. 3), as well as the one of an MMF using the same AMTL and two copies of the same AMR (see Fig. 5). The fabrication flow we have relied on is described in Fig. 9. An HR silicon wafer was used as a substrate. On top of the HR Si wafer, we sputtered an 80-nm-thick Pt layer, followed by a 400-nm-thick AlScN thin film with a $Sc_{\%}$ value of 30% [see Fig. 9(a)]. Later, a SiO_2 hard mask was deposited via CVD and patterned using RIE to form the release windows [see Fig. 9(b)]. Subsequently, the release windows were etched using ICP-RIE, and the SiO_2 hard mask was stripped using hydrofluoric acid [see Fig. 9(c)]. Afterward, a new 2.2-μm-thick SiO_2 layer was deposited and initially patterned to form a buffer layer. This layer allows to decrease the parasitics due to routing [see Fig. 9(d)]. Then, the same oxide layer was patterned again to form the rods [see Fig. 9(e)]. It is worth mentioning that the rods of the reported MMF were made with SiO_2 for two main reasons. First, SiO_2 permits to achieve a degree of temperature compensation [42]. Second, etching SiO_2 can be done with a fluorine-based ICP, which does not etch AlScN. This makes the fabrication of MMFs repeatable and reliable. Subsequently, Al was sputtered and patterned via liftoff to form the input and output transducers [see Fig. 9(f)]. Then, electrical routing and the probing pads were formed by depositing and patterning a 200-nm-thick Au layer [see Fig. 9(g)]. Finally, the device was released using XeF_2 [see Fig. 9(h)]. SEM images of the fabricated MMF, $MMF^{(PML)}$, and $MMF^{(SF)}$ devices are shown in Fig. 9(j)–(l). For all these built structures, we have stacked two identical devices with parallel input and output ports.

B. Experiments

We proceeded with the characterization of the built AMTL, AMR, and MMF by relying on a measured characterization of their S_{21} trends. All the S_{21} trends were extracted using a VNA available in our laboratory and on-chip probes. We first tested

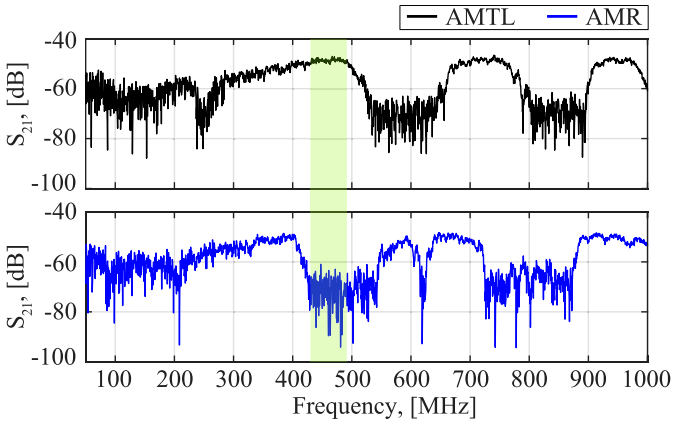

Fig. 10. Measured S_{21} responses of a fabricated AMTL and a fabricated AMR. The highlighted region shows how the deepest stopband of the AMR covers the desired MMF's passband.

the S_{21} of the fabricated AMTL and AMR devices to experimentally verify the existence of their stopbands (see Fig. 10). Both these S_{21} trends versus frequency clearly demonstrate the existence of stopbands. Furthermore, the S_{21} of the AMTL shows a low loss between 475 and 500 MHz, contrasting with the AMRs that exhibit a large attenuation due to their operation in a stopband. As mentioned in Section II, this is a fundamental design condition for MMFs. We report in Fig. 11(a) the transmission of the built MMF achieved using the same AMTL and AMR structures discussed in Fig. 10. As done in our FEM study, we also report the S_{21} trend versus frequency for an MMF using, on behalf of the AMRs, stress-free boundaries or full connections to the silicon substrate. It is worth mentioning that the S_{21} trends reported in Fig. 11(a) were extracted when assuming the use of two identical matching networks (one per port), as described in Fig. 4. These networks include one ideal inductor and one ideal capacitor, with inductance (L_{LM}) and capacitance (C_{LM}) equal to 139 nH and 12 pF, respectively. The S_{21} trends reported in Fig. 11(a) follow the same phenomenological behavior of the corresponding simulated ones (see Fig. 5). In particular, both MMF and MMF$^{(SF)}$ show a loss of 4.9 dB around their center frequency, while MMF$^{(PML)}$ exhibits a loss of 9 dB due to high anchor dissipations. Moreover, all these fabricated devices exhibit a similar out-of-band rejection of ~75 dB for frequencies above the passband. Nonetheless, the MMF shows a higher out-of-band rejection for frequencies below the passband, which is enabled by AMRs' operation in a passband. All in all, the reported MMF's skirt steepness can be quantified by the attenuation rates of 3 dB per 1 MHz on the right-hand side of its passband and 3 dB per 1.5 MHz on the left-hand side of its passband. The in-band group delay of the reported MMF in Fig. 11(a) is extracted as 70 ± 25 ns [see Fig. 11(b)]. The variation of the group delay inside the filter's passband is not as flat as that of the AWLR reported in [18], which is optimized for constant group delay, but it is still considerably flatter than the group delay of the ladder filters discussed in the same study. Fig. 11(c) reports a zoomed-in view of the S_{21} of the MMF reported in Fig. 11(a) when assuming different finite Q values. Comparing the measured MMF performance with the

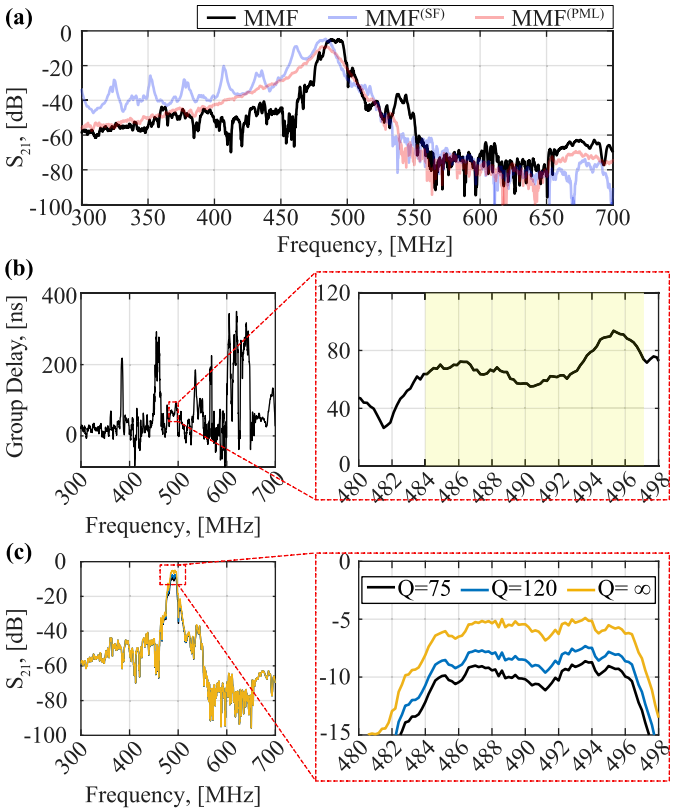

Fig. 11. (a) Measured S_{21} of MMF, MMF$^{(SF)}$, and MMF$^{(PML)}$ when their terminals are matched to 50 Ω using circuit simulated matching networks having the topology depicted in Fig. 4(a). (b) Extracted group delay of the reported MMF in (a). (The highlighted region shows the passband of the MMF.) (c) Zoomed-in view of measured S_{21} responses of MMF when assuming different finite Q values for the matching networks' components.

simulated one in Fig. 5, we observe two main discrepancies: a slightly narrower FBW and a higher loss. The narrower FBW is related to a suboptimal overlapping of AMTL's and AMRs' stopbands/passbands due to process variations. These variations cause a slight shift in the built AMTL's and AMRs' dispersion characteristics. The higher loss is mostly caused by the resistive losses due to electrical routing, specifically at the edges of the buffer oxide layer where, currently, the routing metal strips must climb a 2.2-μm step. We have also created a Table (see Table I) to compare the performance achieved by our built MMF, when assuming a set of matching components with realistic Q values (Q of 75 for inductors and Q of 400 for capacitors), with those attained by previous AWLR filters. As mentioned earlier, AWLR filters also utilize lumped components to create their passband, making them the most suitable current technology for comparison with MMFs. Table I reports center frequency (f_c), insertion loss, FBW, and rejection characteristics of all the previously AWLR filters, together with those of the best MMF reported here. With regards to the rejection capabilities of all the filters listed in Table I, we compared the magnitude of the S_{21} at frequencies that are one bandwidth away (1-BW) and two bandwidths aways (2-BW) from the edge of the passband. We also list the maximum reported rejection for all the filters listed in Table I. Evidently, the reported MMF outperforms all the listed AWLR

TABLE I
COMPARISON OF THE REPORTED MMF WITH PREVIOUSLY REPORTED AWLR FILTERS

Filter	f_c [MHz]	Loss [dB]	FBW [%]	Rejection [dB] 1-BW Away	2-BW Away	Max
This Work	490	8.6	2.54	32	55	75
AWLR (N=3) [18]	418	2.1	0.07	22	33	53
AWLR (N=1), [27]	418	2.4	0.24	12	16	33
AWLR (N=2), [27]	418	5.4	0.12	20	28	60
AWLR (N=1) [28]	417.9	1.25	0.07	11	15	40
AWLR* (N=2) [28]	417.6	1.15	0.24	21	35	56
AWLR (N=3), [29]	418	2	0.08	29	45	50
AWLR (Single-Band), [30]	418	4	0.03	24	30	70

N: Filter Order

*Rejection reported for 2-BW and 3-BW away because of a spurious

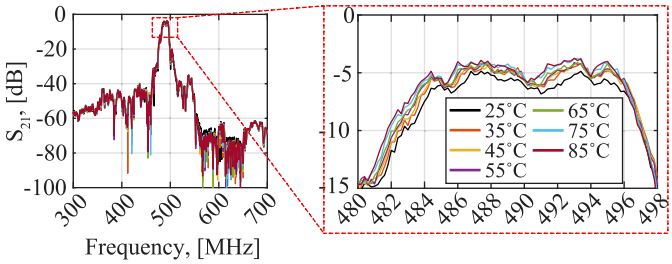

Fig. 12. Measured S_{21} responses of the reported MMF design at different temperatures when their terminals are matched to 50 Ω through circuit simulations using the matching network topology depicted in Fig. 4(a).

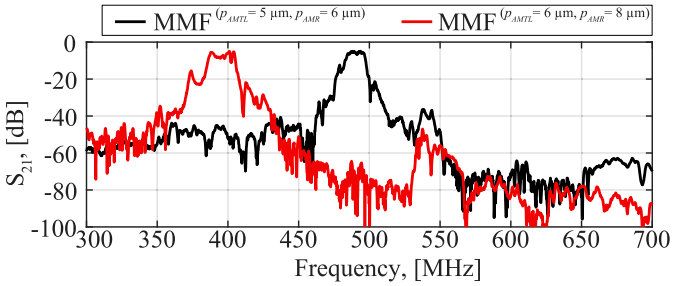

Fig. 13. Measured S_{21} responses of two built MMFs with $p_{\text{AMTL}} = 5\ \mu$m and $p_{\text{AMR}} = 6\ \mu$m, and $p_{\text{AMTL}} = 6\ \mu$m and $p_{\text{AMR}} = 8\ \mu$m, with the terminals matched to 50 Ω using simulated matching networks having the topology depicted in Fig. 4(a).

filters in terms of rejection capabilities (both in 1-BW and 2-BW rejection values and the maximum achievable rejection) and FBW. MMF's loss, on the other hand, is higher than that of the other filters listed in our comparison table. However, loss reductions in MMFs will be possible in the future by increasing C_t, as discussed in Fig. 4. Further loss reductions will be attained by optimizing layout and material composition used for the electrical routing, specifically at the edges of the buffer oxide layer where, currently, routing metal strips must climb a 2.2-μm step.

We also investigated the performance of the MMF shown in Fig. 11 at varying temperatures. During this experiment, the filter was heated on a hot plate up to 85 °C, with 10 °C increments. Meanwhile, the S_{21} was recorded for each temperature increment. The extracted S_{21} trends are reported in Fig. 12. As evident, the filter's passband shifts left as the temperature increases due to a reduction of Young's modulus of the AlScN layer. It is worth mentioning that this reduction is partially compensated from the adoption of the SiO_2 rods, which implement a degree of passive temperature compensation [43], [44]. Based on our measurements, the average TCF of the MMF's center frequency is 22.2 ppm/°C.

As mentioned earlier, the location of the stopbands generated by an AM structure can be tuned by changing the pitch of its unit cell. Therefore, MMFs' center frequency can be lithographically tuned by properly sizing p_{AMTL} and p_{AMR}. To illustrate this feature, we are also reporting the S_{21} trend versus frequency of another built MMF with $p_{\text{AMTL}} = 6\ \mu$m and $p_{\text{AMR}} = 8\ \mu$m (see Fig. 13). This filter utilizes the same matching network topology discussed in Fig. 4, with L_{LM} and C_{LM} selected to be 201 nH and 12 pF, respectively. Moreover, the S_{21} of the MMF discussed in Fig. 11(a) has been reincluded in Fig. 13 to best visualize the MMFs' lithographic frequency tunability. Our second included MMF device exhibits an f_c value of 395 MHz, an FBW of 4.65%, and a minimum loss of 5 dB.

IV. CONCLUSION

This article reports the first prototype of a new type of microacoustic filters relying on piezoelectric AMs built out of a highly doped AlScN layer. We called these filters MMFs. MMFs allow to achieve high levels of out-of-band rejection despite not including any high-Q resonant components. They do so by leveraging the unique dispersion characteristics of AMs. MMFs' high out-of-band rejection is attained while maintaining a very compact size. This is not possible with conventional SAW/BAW ladder filters, which require larger filter sizes or higher filter orders to achieve high out-of-band rejection, ultimately resulting in significant insertion loss. Here, we describe MMFs' principle of operation by using finite-element simulations. Next, we showcase the measured response of two fabricated MMF devices, comparing their performance with those attained by other microacoustic filter technologies that, such as MMFs, use additional electrical lumped components for a proper interface with 50-Ω matched RF devices. While this article reports on the first demonstration of MMFs using an AlScN piezoelectric layer, it is envisioned that the physics of MMFs can be leveraged even when using other piezoelectric materials, such as $LiNbO_3$ or $LiTaO_3$. Finally, it is worth mentioning that AMs can be formed by subwavelength periodic structures, allowing them to possess passbands/stopbands at higher frequencies without requiring high-resolution lithography [40]. Therefore, theoretically, there

is no fundamental limitation in scaling the reported MMF technology to higher frequencies.

Acknowledgment

The authors would like to thank the staff of George J. Kostas Nanoscale Technology and the Manufacturing Research Center, Northeastern University, Boston, MA, USA, and the Center for Nanoscale Systems, Harvard University, Cambridge, MA, USA, for their assistance in the device fabrication.

References

[1] K. Yang et al., "Advanced RF filters for wireless communications," *Chip*, vol. 2, no. 4, Dec. 2023, Art. no. 100058, doi: 10.1016/j.chip.2023.100058.

[2] R. Ruby, "A snapshot in time: The future in filters for cell phones," *IEEE Microw. Mag.*, vol. 16, no. 7, pp. 46–59, Aug. 2015, doi: 10.1016/j.vacuum.2011.03.026.

[3] M. Moreira, J. Bjurström, I. Katardjev, and V. Yantchev, "Aluminum scandium nitride thin-film bulk acoustic resonators for wide band applications," *Vacuum*, vol. 86, no. 1, pp. 23–26, Jul. 2011, doi: 10.1016/j.vacuum.2011.03.026.

[4] A. Ansari, "Single crystalline scandium aluminum nitride: An emerging material for 5G acoustic filters," in *IEEE MTT-S Int. Microw. Symp. Dig.*, Guangzhou, China, May 2019, pp. 1–3, doi: 10.1109/IEEE-IWS.2019.8804148.

[5] Y. Zou et al., "Aluminum scandium nitride thin-film bulk acoustic resonators for 5G wideband applications," *Microsyst. Nanoeng.*, vol. 8, no. 1, pp. 1–7, Nov. 2022, doi: 10.1038/s41378-022-00457-0.

[6] L. Chen et al., "Scandium-doped aluminum nitride for acoustic wave resonators, filters, and ferroelectric memory applications," *ACS Appl. Electron. Mater.*, vol. 5, no. 2, pp. 612–622, Feb. 2023, doi: 10.1021/acsaelm.2c01409.

[7] A. Lozzi, E. T.-T. Yen, P. Muralt, and L. G. Villanueva, "$Al_{0.83}Sc_{0.17}N$ contour-mode resonators with electromechanical coupling in excess of 4.5%," *IEEE Trans. Ultrason., Ferroelectr., Freq. Control*, vol. 66, no. 1, pp. 146–153, Jan. 2019, doi: 10.1109/TUFFC.2018.2882073.

[8] G. Esteves et al., "$Al_{0.68}Sc_{0.32}N$ Lamb wave resonators with electromechanical coupling coefficients near 10.28%," *Appl. Phys. Lett.*, vol. 118, no. 17, 2021, Art. no. 171902, doi: 10.1063/5.0047647.

[9] L. Colombo, A. Kochhar, C. Xu, G. Piazza, S. Mishin, and Y. Oshmyansky, "Investigation of 20% scandium-doped aluminum nitride films for MEMS laterally vibrating resonators," in *Proc. IEEE Int. Ultrason. Symp. (IUS)*, Sep. 2017, pp. 1–4.

[10] Z. Lu and Y. Dong, "SAW filter with high out-of-band rejection using improved grounding method," in *IEEE MTT-S Int. Microw. Symp. Dig.*, Qingdao, China, May 2023, pp. 1–3, doi: 10.1109/iws58240.2023.10222703.

[11] O. L. Balysheva, "SAW filters for mobile communications: Achievements and prospects," in *Proc. Wave Electron. Appl. Inf. Telecommun. Syst. (WECONF)*, Saint-Petersburg, Russia, Jun. 2019, pp. 1–4, doi: 10.1109/WECONF.2019.8840661.

[12] J. Liang, H. X. Zhang, D. H. Zhang, H. Zhang, and W. Pang, "50Ω-terminated ALN MEMS filters based on Lamb wave resonators," in *Proc. 18th Int. Conf. Solid-State Sens., Actuators Microsyst. (TRANSDUCERS)*, Anchorage, AK, USA, Jun. 2015, pp. 1973–1976, doi: 10.1109/TRANSDUCERS.2015.7181340.

[13] C. Cassella, G. Chen, Z. Qian, G. Hummel, and M. Rinaldi, "RF passive components based on aluminum nitride cross-sectional Lamé-mode MEMS resonators," *IEEE Trans. Electron Devices*, vol. 64, no. 1, pp. 237–243, Jan. 2017, doi: 10.1109/TED.2016.2621660.

[14] G. Chen, C. Cassella, T. Wu, and M. Rinaldi, "Single-chip multi-frequency wideband filters based on aluminum nitride cross-sectional Lamé mode resonators with thick and apodized electrodes," in *Proc. IEEE Micro Electro Mech. Syst. (MEMS)*, Belfast, Ireland, Jan. 2018, pp. 775–778, doi: 10.1109/MEMSYS.2018.8346670.

[15] Z. Schaffer and G. Piazza, "Investigation of damping and ladder filter synthesis for 3 GHz 20% scandium-doped aluminum nitride cross-sectional lame mode resonators," in *Proc. IEEE Int. Ultrason. Symp. (IUS)*, Las Vegas, NV, USA, Sep. 2020, pp. 1–4, doi: 10.1109/IUS46767.2020.9251790.

[16] S. Nam et al., "A mm-wave trilayer AlN/ScAlN/AlN higher order mode FBAR," *IEEE Microw. Wireless Technol. Lett.*, vol. 33, no. 6, pp. 803–806, Jun. 2023, doi: 10.1109/LMWT.2023.3271865.

[17] V. Chulukhadze et al., "Frequency scaling millimeter wave acoustic resonators using ion beam trimmed lithium niobate," in *Proc. Joint Conf. Eur. Freq. Time Forum IEEE Int. Freq. Control Symp. (EFTF/IFCS)*, Toyama, Japan, May 2023, pp. 1–4, doi: 10.1109/eftf/ifcs57587.2023.10272038.

[18] D. Psychogiou, R. Gómez-Garda, and D. Peroulis, "RF design of acoustic-wave-lumped-element-resonator-(AWLR)-based bandpass filters with constant in-band group delay," in *IEEE MTT-S Int. Microw. Symp. Dig.*, Jun. 2017, pp. 1472–1475, doi: 10.1109/MWSYM.2017.8058899.

[19] M. Rinaldi, C. Zuniga, C. Zuo, and G. Piazza, "Ultra-thin super high frequency two-port ALN contour-mode resonators and filters," in *Proc. Int. Solid-State Sens., Actuators Microsyst. Conf.*, Denver, CO, USA, Jun. 2009, pp. 577–580, doi: 10.1109/SENSOR.2009.5285390.

[20] C.-M. Lin, Y.-Y. Chen, V. V. Felmetsge, D. G. Senesky, and A. P. Pisano, "Two-port filters and resonators on AlN/3C-SiC plates utilizing high-order Lamb wave modes," in *Proc. IEEE 26th Int. Conf. Micro Electro Mech. Syst. (MEMS)*, Taiwan, Jan. 2013, pp. 789–792, doi: 10.1109/MEMSYS.2013.6474361.

[21] J. Meltaus and T. Pensala, "Laterally coupled BAW filter using two acoustic modes," in *Proc. IEEE Int. Ultrason. Symp. (IUS)*, Prague, Czech Republic, Jul. 2013, pp. 232–235, doi: 10.1109/ULTSYM.2013.0060.

[22] T. Pensala, T. Makkonen, J. Dekker, and M. Ylilammi, "Laterally acoustically coupled BAW filters at 3.6 GHz," in *Proc. IEEE Int. Ultrason. Symp. (IUS)*, Kobe, Japan, Oct. 2018, pp. 1–4, doi: 10.1109/ULTSYM.2018.8579900.

[23] G. G. Fattinger, R. Aigner, and W. Nessler, "Coupled bulk acoustic wave resonator filters: Key technology for single-to-balanced RF filters," in *IEEE MTT-S Int. Microw. Symp. Dig.*, vol. 2, Forth Worth, TX, USA, Jun. 2004, pp. 927–929, doi: 10.1109/MWSYM.2004.1339126.

[24] K. M. Lakin, "Coupled resonator filters," in *Proc. IEEE Ultrason. Symp.*, Munich, Germany, Oct. 2002, pp. 901–908, doi: 10.1109/ULTSYM.2002.1193543.

[25] A. A. Shirakawa, J.-M. Pham, P. Jarry, and E. Kerherve, "Bulk acoustic wave coupled resonator filters synthesis methodology," in *Proc. Eur. Microw. Conf.*, Paris, France, 2005, p. 4, doi: 10.1109/EUMC.2005.1608915.

[26] A. A. Shirakawa, R. Thalhammer, T. Jamneala, and U. B. Koelle, "Bulk acoustic wave-coupled resonator filters: Concept, design, and application," *Int. J. RF Microw. Comput.-Aided Eng.*, vol. 21, no. 5, pp. 477–485, Sep. 2011, doi: 10.1002/mmce.20552.

[27] D. Psychogiou, R. Gómez-García, and D. Peroulis, "Coupling-Matrix-Based design of high-Q bandpass filters using acoustic-wave lumped-element resonator (AWLR) modules," *IEEE Trans. Microw. Theory Techn.*, vol. 63, no. 12, pp. 4319–4328, Dec. 2015, doi: 10.1109/TMTT.2015.2494597.

[28] D. Psychogiou, R. Gómez-García, R. Loeches-Sánchez, and D. Peroulis, "Hybrid acoustic-wave-lumped-element resonators (AWLRs) for high-Q bandpass filters with quasi-elliptic frequency response," *IEEE Trans. Microw. Theory Techn.*, vol. 63, no. 7, pp. 2233–2244, Jul. 2015, doi: 10.1109/TMTT.2015.2438894.

[29] D. Psychogiou, R. Gómez-García, and D. Peroulis, "Single and multiband acoustic-wave-lumped- element-resonator (AWLR) bandpass filters with reconfigurable transfer function," *IEEE Trans. Microw. Theory Techn.*, vol. 64, no. 12, pp. 4394–4404, Dec. 2016, doi: 10.1109/TMTT.2016.2617884.

[30] N. S. Luhrs, D. J. Simpson, and D. Psychogiou, "Multiband acoustic-wave-lumped-element resonator-based bandpass-to-bandstop filters," *IEEE Microw. Wireless Compon. Lett.*, vol. 29, no. 4, pp. 261–263, Apr. 2019, doi: 10.1109/LMWC.2019.2901199.

[31] S. A. Cummer, J. Christensen, and A. Alù, "Controlling sound with acoustic metamaterials," *Nature Rev. Mater.*, vol. 1, no. 3, pp. 1–13, Feb. 2016, doi: 10.1038/natrevmats.2016.1.

[32] N. Fang et al., "Ultrasonic metamaterials with negative modulus," *Nature Mater.*, vol. 5, no. 6, pp. 452–456, Jun. 2006, doi: 10.1038/nmat1644.

[33] Z. Yang, J. Mei, M. Yang, N. H. Chan, and P. Sheng, "Membrane-type acoustic metamaterial with negative dynamic mass," *Phys. Rev. Lett.*, vol. 101, no. 20, Nov. 2008, Art. no. 204301, doi: 10.1103/physrevlett.101.204301.

[34] X. Zhu, B. Liang, W. Kan, X. Zou, and J. Cheng, "Acoustic cloaking by a superlens with single-negative materials," *Phys. Rev. Lett.*, vol. 106, no. 1, Jan. 2011, Art. no. 014301, doi: 10.1103/physrevlett.106.014301.

[35] M. D. Guild, M. R. Haberman, and A. Alù, "Plasmonic-type acoustic cloak made of a bilaminate shell," *Phys. Rev. B*, vol. 86, no. 10, Sep. 2012, Art. no. 104302, doi: 10.1103/physrevb.86.104302.

[36] R. Ardito, C. Comi, V. Zega, and A. Corigliano, "Metamaterials and MEMS (MetaMEMS): A promising trend in microsystems technology," in *Proc. 24th Int. Conf. Thermal, Mech. Multi-Phys. Simulation Exp. Microelectron. Microsyst. (EuroSimE)*, Apr. 2023, pp. 1–4, doi: 10.1109/EuroSimE56861.2023.10100824.

[37] J. Li, L. Fok, X. Yin, G. Bartal, and X. Zhang, "Experimental demonstration of an acoustic magnifying hyperlens," *Nature Mater.*, vol. 8, no. 12, pp. 931–934, Dec. 2009, doi: 10.1038/nmat2561.

[38] C. M. Park, J. J. Park, S. H. Lee, Y. M. Seo, C. K. Kim, and S. H. Lee, "Amplification of acoustic evanescent waves using metamaterial slabs," *Phys. Rev. Lett.*, vol. 107, no. 19, Nov. 2011, Art. no. 194301, doi: 10.1103/physrevlett.107.194301.

[39] X. Zhao, L. Colombo, and C. Cassella, "Aluminum nitride two-dimensional-resonant-rods," *Appl. Phys. Lett.*, vol. 116, no. 14, Apr. 2020, Art. no. 143504, doi: 10.1063/5.0005203.

[40] X. Zhao et al., "A 5.3 GHz $Al_{0.76}Sc_{0.24}N$ two-dimensional resonant rods resonator with a k_t^2 of 23.9%," *J. Microelectromech. Syst.*, vol. 31, no. 4, pp. 561–570, Aug. 2022, doi: 10.1109/jmems.2022.3178978.

[41] X. Zhao, O. Kaya, M. Pirro, P. Simeoni, J. Segovia-Fernandez, and C. Cassella, "Extending the linearity of AlScN contour-mode-resonators through acoustic metamaterials-based reflectors," *IEEE Trans. Ultrason., Ferroelectr., Freq. Control*, vol. 70, no. 10, pp. 1229–1238, Oct. 2023, doi: 10.1109/TUFFC.2023.3245809.

[42] X. Zhao, O. Kaya, T. Maggioli, and C. Cassella, "Multipurpose acoustic metamaterial anchors for aluminum scandium nitride contour mode resonators," *J. Microelectromech. Syst.*, early access, May 16, 2024, doi: 10.1109/JMEMS.2024.3399593.

[43] C.-M. Lin et al., "Experimental study of temperature-compensated aluminum nitride Lamb wave resonators," in *Proc. IEEE Int. Freq. Control Symp. Joint 22nd Eur. Freq. Time Forum*, Apr. 2009, pp. 5–9, doi: 10.1109/FREQ.2009.5168132.

[44] C.-M. Lin, T.-T. Yen, V. V. Felmetsger, M. A. Hopcroft, J. H. Kuypers, and A. P. Pisano, "Thermal compensation for aluminum nitride Lamb wave resonators operating at high temperature," in *Proc. IEEE Int. Freq. Control Symp.*, Jun. 2010, pp. 14–18, doi: 10.1109/FREQ.2010.5556381.

Onurcan Kaya (Graduate Student Member, IEEE) received the B.S. and M.S. degrees in mechanical engineering from Middle East Technical University (METU), Ankara, Türkiye, in 2014 and 2017, respectively. He is currently pursuing the Ph.D. degree with the Department of Electrical and Computer Engineering, Northeastern University, Boston, MA, USA.

His research interests include the design, fabrication, and characterization of MEMS devices, particularly capacitive resonant sensors, piezoelectric microacoustic resonators, piezoelectric microacoustic filters, and ferroelectric varactors.

Xuanyi Zhao (Graduate Student Member, IEEE) received the B.S. degree in applied physics from Xi'an Jiaotong University (XJTU), Xi'an, China, in 2015. He is currently pursuing the Ph.D. degree with the Department of Electrical and Computer Engineering, Northeastern University, Boston, MA, USA.

One of his previous journal articles was selected as a featured article by the *Applied Physics Letters* magazine. His current research interests include microacoustic radio frequency (RF) devices based on piezoelectric acoustic metamaterials (AMs).

Mr. Zhao won the Best Paper Award at the IEEE International Frequency Control Symposium (IFCS), Paris, in 2022.

Cristian Cassella (Member, IEEE) received the B.S.E. and M.Sc. degrees (Hons.) from the University of Rome Tor Vergata, Rome, Italy, in 2006 and 2009, respectively, and the Ph.D. degree from Carnegie Mellon University, Pittsburgh, PA, USA, in 2015.

In 2011, he was a Visiting Scholar with the University of Pennsylvania, Philadelphia, PA, USA. In 2015, he was a Postdoctoral Research Associate with Northeastern University, Boston, MA, USA. In 2018, he became an Assistant Professor. He is currently an Associate Professor with the Electrical and Computer Engineering Department, Northeastern University. He is the author of more than 100 publications in peer-reviewed journals and conference proceedings. Two of his peer-reviewed journal articles published on the IEEE JOURNAL OF MICROELECTROMECHANICAL SYSTEMS (JMEMS) were selected as the Papers of Excellent Quality (JMEMS RightNowPapers), hence being released as open access. One of his journal articles was chosen as the cover for the *Nature Nanotechnology* October 2017 Issue. Another one of his journal articles was selected as a featured article by the *Applied Physics Letters* magazine. He holds seven patents and four patent applications in the area of acoustic resonators and RF systems.

Dr. Cassella was awarded the Marie Sklodowska-Curie Individual Fellowship by European Community (EU) in 2018. In 2021, he was a recipient of the NSF CAREER Award. He received the Best Student Paper Award at the IEEE International Frequency Control Symposium in 2013, and in 2021, 2022, and 2023 (with his students). He is a Technical Reviewer of several journals, such as *Applied Physics Letters*, IEEE TRANSACTIONS ON ELECTRON DEVICES, IEEE TRANSACTIONS ON ULTRASONICS, FERROELECTRICS, AND FREQUENCY CONTROL, IEEE JOURNAL OF MICROELECTROMECHANICAL SYSTEMS, IEEE ELECTRON DEVICE LETTERS, *Journal of Micromechanics and Microengineering*, *Journal of Applied Physics*, IEEE SENSORS LETTERS, and *Review of Scientific Instruments*.